

Article

Hydrothermal Synthesis of Co-Doped NiSe₂ Nanowire for High-Performance Asymmetric Supercapacitors

Yun Gu, Le-Qing Fan * , Jian-Ling Huang, Cheng-Long Geng, Jian-Ming Lin, Miao-Liang Huang, Yun-Fang Huang and Ji-Huai Wu

Engineering Research Center of Environment-Friendly Functional Materials, Ministry of Education, College of Materials Science and Engineering, Huaqiao University, Xiamen 361021, China; 1611302006@hqu.edu.cn (Y.G.); 1611302010@hqu.edu.cn (J.-L.H.); 17013081007@hqu.edu.cn (C.-L.G.); jmlin@hqu.edu.cn (J.-M.L.); huangml@hqu.edu.cn (M.-L.H.); huangyf@hqu.edu.cn (Y.-F.H.); jhwu@hqu.edu.cn (J.-H.W.)

* Correspondence: leqingfan@163.com; Tel.: +86-592-616-2221

Received: 20 June 2018; Accepted: 15 August 2018; Published: 18 August 2018



Abstract: Co@NiSe₂ electrode materials were synthesized via a simple hydrothermal method by using nickel foam in situ as the backbone and subsequently characterized by scanning electron microscopy, transmission electron microscopy, energy-dispersive X-ray spectroscopy, and a specific surface area analyzer. Results show that the Co@NiSe₂ electrode exhibits a nanowire structure and grows uniformly on the nickel foam base. These features make the electrode show a relatively high specific surface area and electrical conductivity, and thus exhibit excellent electrochemical performance. The obtained electrode has a high specific capacitance of 3167.6 F·g⁻¹ at a current density of 1 A·g⁻¹. To enlarge the potential window and increase the energy density, an asymmetric supercapacitor was assembled by using a Co@NiSe₂ electrode and activated carbon acting as positive and negative electrodes, respectively. The prepared asymmetrical supercapacitor functions stably under the potential window of 0–1.6 V. The asymmetric supercapacitor can deliver a high energy density of 50.0 Wh·kg⁻¹ at a power density of 779.0 W·kg⁻¹. Moreover, the prepared asymmetric supercapacitor exhibits a good rate performance and cycle stability.

Keywords: Co-doped NiSe₂; nanowire; hydrothermal method; pseudocapacitance; asymmetric supercapacitors

1. Introduction

Supercapacitors are excellent energy-storage devices which are attracting increased research attention. Although lithium-ion batteries or nickel–metal hydride batteries have a high energy density, their charge and discharge rates are relatively slow and cannot meet the needs of modern life [1]. People are eagerly pursuing energy-storage devices with high energy densities and high power densities simultaneously [2,3]. Compared with traditional batteries, supercapacitors have a high power density, high charge and discharge rates, a wide operating temperature range, environmental protection, and a long cycle life [4,5]. Therefore, they have been widely used in portable electronics, power backup, electric vehicles, various microdevices, and other fields [6].

However, an issue related to the supercapacitors is the lower energy density compared with battery systems or fuel cells [7]. According to the calculation formula for the energy density of the supercapacitor: $E = 1/2CV^2$, the energy density (E) can be evaluated by the specific capacitance (C_s) and the cell voltage (V). To further increase the energy density, considering both the advantages of supercapacitors (rate, cycle life) and advanced batteries (energy density), assembly

of an asymmetric supercapacitor is a commonly used strategy, where the electrode materials with high pseudocapacitance can be employed and the operating voltage can be expanded [8,9]. However, the key to preparing asymmetrical supercapacitors is the selection of suitable positive and negative materials that can function stably under different potential windows in the same electrolyte [10]. This condition is important for the design and preparation of positive and negative materials for asymmetric supercapacitors. Carbon-based materials, such as graphene, activated carbon (AC), carbon fiber, and carbon nanotubes are used as negative materials due to their high electrical conductivity, high specific surface area, good thermal stability, corrosion resistance, controllable pore structure, and other unique physical and chemical properties [11–13]. Among them, AC is generally chosen as the negative electrode material of asymmetric supercapacitors due to the advantages of a high specific surface area, low cost, and stable performance [14].

Recently, increasing attention has been paid to transition metal sulfides as they exhibit a higher theoretical capacitance and better electric conductivity than transition metal oxides [15]. The charge storage mechanisms and the electrochemical properties of transition metal sulfides, such as Ni_3S_4 , CoS , MoS_2 , and CuS , have been widely studied as electrode materials in supercapacitors or asymmetric supercapacitors. However, due to the volume change of sulfide electrode materials during charging and discharging, they are easily detached from the current collectors, which affects their electrochemical performances [16]. Therefore, finding a good material becomes a challenge [17]. Although metal selenide also belongs to the metal chalcogen compounds and can produce a high pseudocapacitance, few reports on the use of metal selenides in supercapacitors are available to date. The published works indicate that selenide has a high theoretical specific capacitance and good electrochemical performance. For example, Wang et al. [18] prepared a cubic NiSe_2 electrode material under hydrothermal conditions, showing a specific capacitance of $1044 \text{ F}\cdot\text{g}^{-1}$ at $3 \text{ A}\cdot\text{g}^{-1}$. Recently, Huang et al. [19] reported a layered MoSe_2 nanosheet electrode material prepared on a Ni foam substrate by a simple hydrothermal method exhibiting a high specific capacitance of $1114.3 \text{ F}\cdot\text{g}^{-1}$ at $1 \text{ A}\cdot\text{g}^{-1}$ and excellent cycle life due to its specific structure. Zhang et al. [20] prepared a unique double-shelled hollow structure CoSe_2/C composite with heterogeneous intervals between the two shells with a high specific capacitance of $726 \text{ F}\cdot\text{g}^{-1}$ at $2 \text{ A}\cdot\text{g}^{-1}$.

To further obtain a selenide electrode material with superior electrochemical performances, we attempt to dope using a pseudocapacitive metal ion, which may lead to a greater abundance in the redox reactions to produce a high capacitance, and an improvement in the electrochemical performances due to the complementary advantages of a doped metal ion and the synergistic effects of the doped metal ion and the host ions.

In this article, Co^{2+} was doped in situ into a NiSe_2 electrode material (Co@NiSe_2) grown on Ni foam using a simple hydrothermal method. The prepared Co@NiSe_2 electrode material has a specific capacitance of $3167.6 \text{ F}\cdot\text{g}^{-1}$ at a current density of $1 \text{ A}\cdot\text{g}^{-1}$ in 3 M KOH aqueous solution. Using the Co@NiSe_2 electrode material as the positive electrode and AC as the negative electrode, an asymmetric supercapacitor was assembled to increase the potential window and the energy density [21,22]. The energy density reaches $50 \text{ Wh}\cdot\text{kg}^{-1}$ at a power density of $779 \text{ W}\cdot\text{kg}^{-1}$. Thus, the asymmetric supercapacitor exhibits good electrochemical performance and stable cycle life.

2. Experimental Section

2.1. Materials

Anhydrous ethanol, acetone, 60% aqueous solution of polytetrafluoroethylene (PTFE), urea ($\text{CH}_4\text{N}_2\text{O}$), and acetylene black were purchased from Sinopharm Group Chemical Reagent Co., Ltd. (Shanghai, China). Cobalt chloride hexahydrate ($\text{CoCl}_2\cdot 6\text{H}_2\text{O}$), Nickel chloride hexahydrate ($\text{NiCl}_2\cdot 6\text{H}_2\text{O}$), and selenium dioxide (SeO_2) were available from Aladdin Industrial Corporation (Shanghai, China). Nickel foam was purchased from Changsha Liyuan New Material Company (Changsha, China). AC was purchased from Fuzhou Yihuan Co., Ltd. (Fuzhou, China). All materials are commercially available and do not require further purification.

2.2. Preparation of Co@NiSe₂

To remove the oxide layer and other impurities on the surface of the nickel foam, the nickel foam was sonicated in acetone for 2 h, followed by ultrasonication with anhydrous ethanol for 2 h, repeated washing with distilled water, drying, and allowed to stand. To make the electrode material grow stably and uniformly on the nickel foam, before the reaction, we trimmed the treated nickel foam to $1 \times 1 \text{ cm}^2$ and placed it in a plasma cleaner (PDC-001, Xmcreat, Xiamen, China) for 2 min for secondary treatment.

Here, we synthesized a Co@NiSe₂ electrode material using a simple hydrothermal method. First, 1 mmol of NiCl₂·6H₂O and 2 mmol of SeO₂ were dissolved in 50 ml of deionized water and stirred until they completely dissolved. Next, 15 mmol CH₄N₂O was added and continuously stirred at room temperature for 30 min. Then, a certain amount of CoCl₂·6H₂O was added to obtain a uniformly dispersed mixed solution. After the secondary treatment, nickel foam was stably suspended in a Teflon-lined stainless-steel autoclave with a capacity of 100 mL, and the above dispersed mixed solution was transferred into the autoclave. Subsequently, the autoclave was sealed in an electric oven at 180 °C for 16 h. After the hydrothermal process was completed, the nickel foam carrying the active material was taken out and washed several times with distilled water and ethanol. After drying in a vacuum oven at 80 °C for 12 h, a Co@NiSe₂ electrode material was finally obtained, and the loading of the active material was approximately $2.5 \text{ mg}\cdot\text{cm}^{-2}$. The samples were named NiSe₂, Co@NiSe₂-1, Co@NiSe₂-2, and Co@NiSe₂-3 for the addition of 0, 1, 2, and 3 mmol CoCl₂·6H₂O, respectively.

2.3. Assembly of Asymmetrical Supercapacitors

Here, we used the prepared nickel foam loaded with the Co@NiSe₂ electrode material as a positive electrode, AC as a negative electrode, and 3 M KOH aqueous solution as an electrolyte to assemble asymmetrical supercapacitors. First, we prepared a negative active carbon by a typical method [23]. AC, acetylene black, and polytetrafluoroethylene were dispersed in an appropriate amount of absolute ethanol at a mass ratio of 8:1:1, and the resulting mixture was sonicated for 2 h and then dried in an oven at 80 °C. Excess ethanol was volatilized off, and the mixture was stirred into gel form. Then, the gel-like AC was pressed into a sheet using a roller press. The appropriate amount of AC was cut according to the required amount, and the cut AC sheet was pressed under pressure onto the treated nickel foam and dried in a vacuum oven at 80 °C for 12 h to obtain an AC negative electrode [24].

The most critical problem in the construction of asymmetric supercapacitors is the active material mass matching of the positive and negative electrodes. Without considering the energy loss due to internal resistance in an ideal state, when the capacitor was charged and discharged, the charge conservation principle was used for the calculation, illustrated as follows [25]:

$$q = C_s \times \Delta E \times m \quad (1)$$

From Formula (1), the charge storage capacity mainly depends on the mass-specific capacitance of the electrode (C_s), voltage during charge/discharge (ΔE), and the active material mass (m) of the electrode. To conserve the charge of both positive and negative levels ($q^+ = q^-$), the mass ratio of positive (m^+) and negative (m^-) electrodes follows Equation (2) [26]:

$$\frac{m_+}{m_-} = \frac{C_- \times \Delta V_-}{C_+ \times \Delta V_+} \quad (2)$$

2.4. Material Characterization

Phase analysis of the prepared samples was performed on an X-ray powder diffractometer (XRD, CuK α radiation, Bruker D8 Advance, Karlsruhe, Germany). The microstructure and morphology of the Co@NiSe₂ electrode material were observed through field emission scanning electron microscopy (FESEM, S-4800, Hitachi, Tokyo, Japan) and transmission electron microscopy (TEM, H-7650, Hitachi,

Tokyo, Japan). Using energy-dispersive X-ray spectroscopy (EDS, INCA Energy, Shanghai, China), the elements of the sample were qualitatively analyzed. The specific surface area and pore size distribution of the samples were determined by a fully automatic specific surface area analyzer (BET, Autosorb-iQ, Atlanta, GA, USA).

2.5. Electrochemical Measurements

The most effective way to measure the performance of the supercapacitor is to test the electrochemical performance of the electrode material. At room temperature, we used the 3 M KOH aqueous solution as the electrolyte, the platinum wire electrode as the counter electrode, the saturated calomel electrode as the reference electrode, and Co@NiSe₂ on nickel foam was used as the working electrode. Using an electrochemical workstation (CHI760E, Shanghai Chenhua Instrument, Shanghai, China), cyclic voltammetry (CV), galvanostatic charge–discharge (GCD) test, electrochemical impedance spectroscopy (EIS), and cycle life testing were performed on the electrode material.

In general, the capacitance of a supercapacitor reflects the ability to store charge, mainly reflecting the properties of the electrode material. The GCD test was used to calculate the specific capacitance (C_s) of the supercapacitor according to Equation (3) [27]:

$$C_s = \frac{i}{m} \int \frac{v dt}{\frac{v^2}{2} \Big|_{v_i}^{v_f}} \quad (3)$$

where C_s (F g⁻¹) is the specific capacitance; I (A) is the current during discharge; Δt (s) is the discharge time; m (g) is the mass of the active material; and ΔV (V) is the potential during the discharge process.

Energy density (E) is an indicator of the performance of a supercapacitor and can directly reflect the capacitor's ability to store charge. The energy density is related to the specific capacitance of the capacitor and the discharge voltage window as illustrated in Formula (4) [28]:

$$E = \frac{C_s \Delta V^2}{7.2} \quad (4)$$

The power density (P) is another key index that determines the rapid charge and discharge capacity of a capacitor by Formula (5) [29]:

$$P = \frac{3600E}{\Delta t} \quad (5)$$

3. Results and Discussion

3.1. Characterization of Electrode Materials

To accurately show the structure of the prepared electrode material, we performed an XRD test. Figure 1a shows the blank nickel foam, NiSe₂, and Co@NiSe₂-2 electrode materials. The XRD pattern, wherein “♦” represents the three very strong peaks (44.5°, 51.8°, and 76.37°), displays the nickel-foam base (JCPDS no. 04-0850). In addition to the nickel base peaks, the NiSe₂ diffraction peaks (JPDS no. 41-1495) are 29.79°, 33.40°, 36.70°, 50.48°, and 57.52°, corresponding to the (200), (210), (211), (311), and (230) crystal planes, respectively. In the XRD pattern of Co@NiSe₂-2, we find a slight shift in the spectrum presumably due to a small amount of Co doping. In addition, the chemical composition of the synthesized product was characterized using EDS analysis, as shown in Figure 1b. The information on Ni, Se, and Co can be seen from the figure, and the surface sample was composed of the above elements. Moreover, the displayed oxygen may come from the oxygen and moisture on the sample surface.

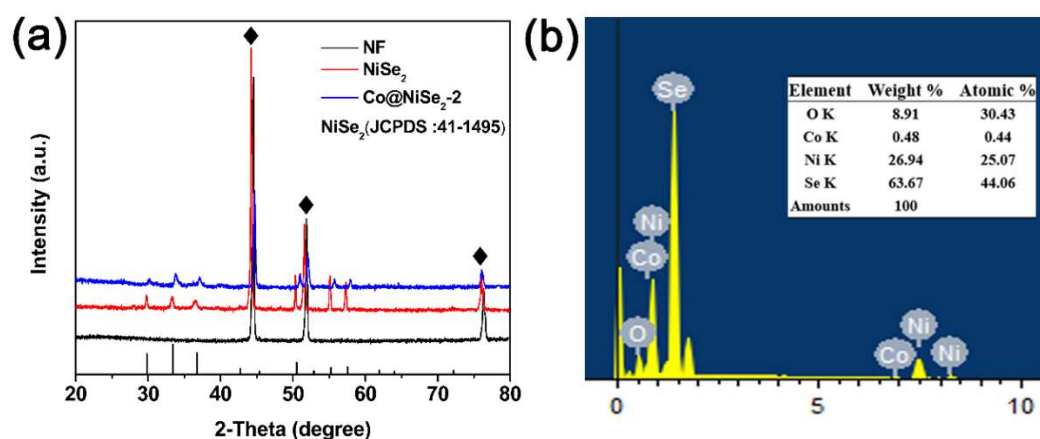


Figure 1. (a) X-ray diffraction (XRD) patterns of blank nickel foam (NF), NiSe₂, and Co@NiSe₂-2; (b) energy-dispersive X-ray spectroscopy (EDS) spectrum of Co@NiSe₂-2.

Figure 2 shows FESEM images of the NiSe₂ and Co@NiSe₂ electrode materials and TEM images of Co@NiSe₂-2 at different magnifications. As presented in Figure 2a,b, under this hydrothermal condition, a NiSe₂ nanowire with a width of about 50 nm can be formed. It is observed that it is possible to retain the morphology after doping with Co²⁺, and increased doping with Co²⁺ results in a decreasing width of the wire (Figure 2c–f). However, for Co@NiSe₂-3, the sample exhibits serious aggregation (Figure 2g–h). Figure 2i also proves that the morphology of Co@NiSe₂-2 is a nanowire with the width of about 20 nm. Two different crystal faces are seen from the analysis of Figure 2j. The interplanar spacings are $d = 0.268$ nm and $d = 0.1806$ nm, corresponding to the (210) and (311) crystal faces of the NiSe₂ crystal, respectively. The hydrothermal synthesis of the nanowire structures can greatly increase the specific surface area of the electrode material, effectively increasing the ion transport process and contributing to a higher specific capacitance.

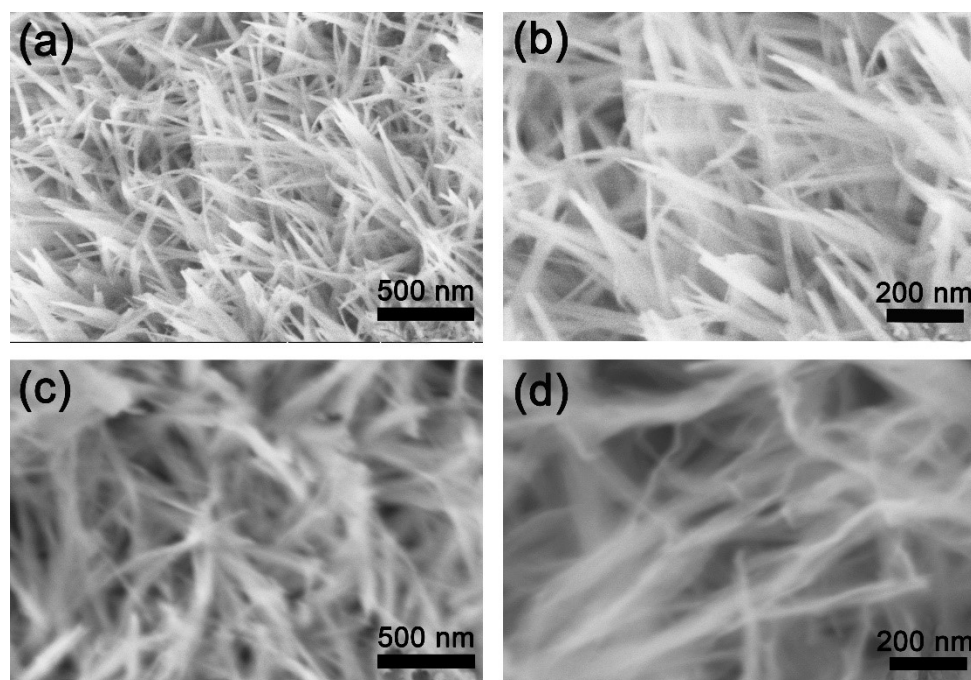


Figure 2. Cont.

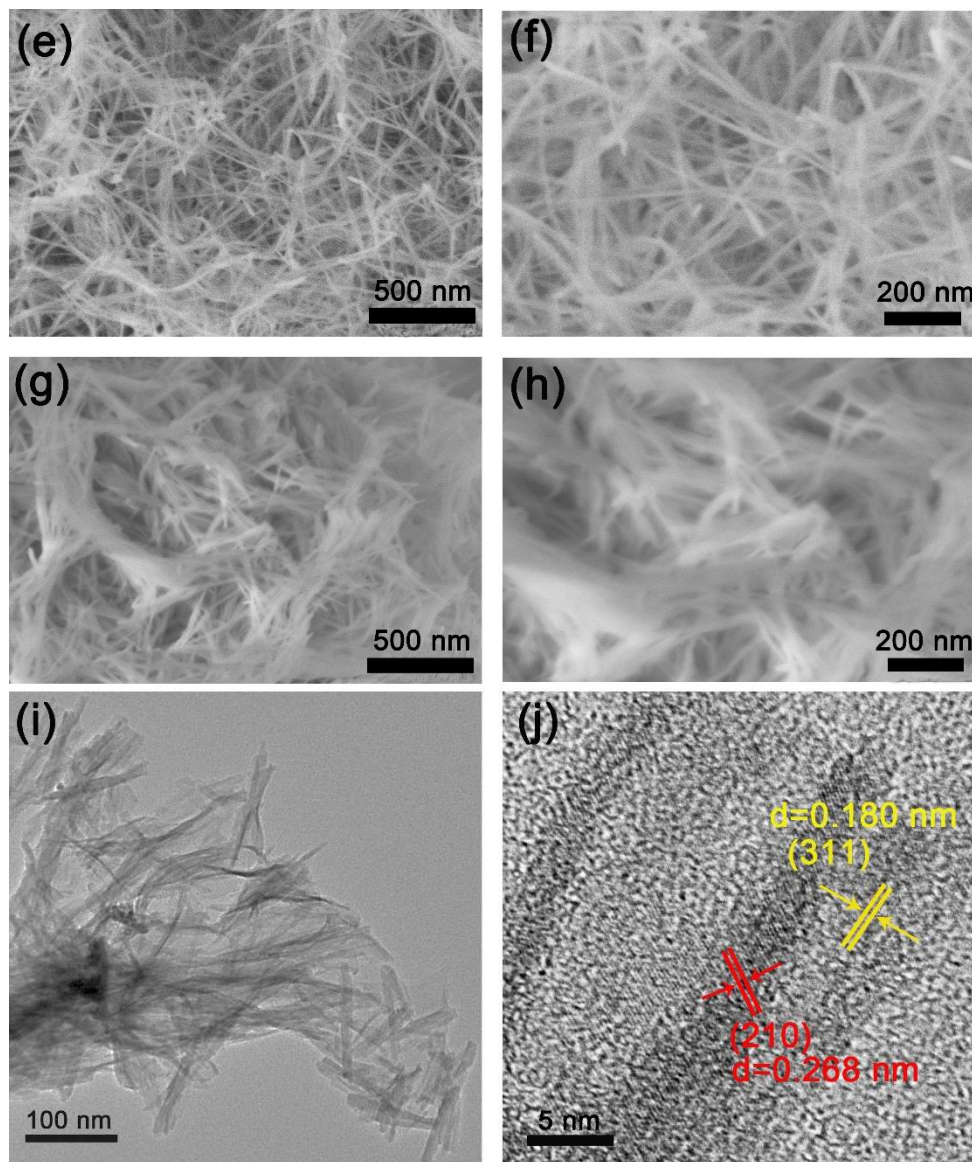


Figure 2. Field emission scanning electron microscopy (FESEM) images of (a,b) NiSe₂; (c,d) Co@NiSe₂-1; (e,f) Co@NiSe₂-2; (g,h) Co@NiSe₂-3; (i,j) transmission electron microscopy (TEM) images of Co@NiSe₂-2 electrode materials.

To study the structure and specific surface area of the nanowires of the electrode material in depth, physical adsorption of nitrogen was used [30]. Figure 3 shows the N₂ adsorption–desorption curves and pore size distributions of the prepared samples. Their specific surface areas, pore volumes and pore sizes are listed in Table 1. The adsorption–desorption curves of NiSe₂, Co@NiSe₂-1, Co@NiSe₂-2, and Co@NiSe₂-3 electrode materials all show the IUPAC-H3 hysteresis loop, which is a type of BDDT-IV and belongs to a typical mesoporous structure [31]. The results show that with the increase of the Co²⁺ content of the reactant, the specific surface area increases from 54.6 m²·g⁻¹ to the maximum value of 135.2 m²·g⁻¹ (Co@NiSe₂-2), before decreasing to 11.5 m²·g⁻¹ (Co@NiSe₂-3). The reason for the enhancement of the specific surface area can be attributed to the thinner nanowire [32]. However, the aggregation leads to the decrement of the specific surface area for Co@NiSe₂.

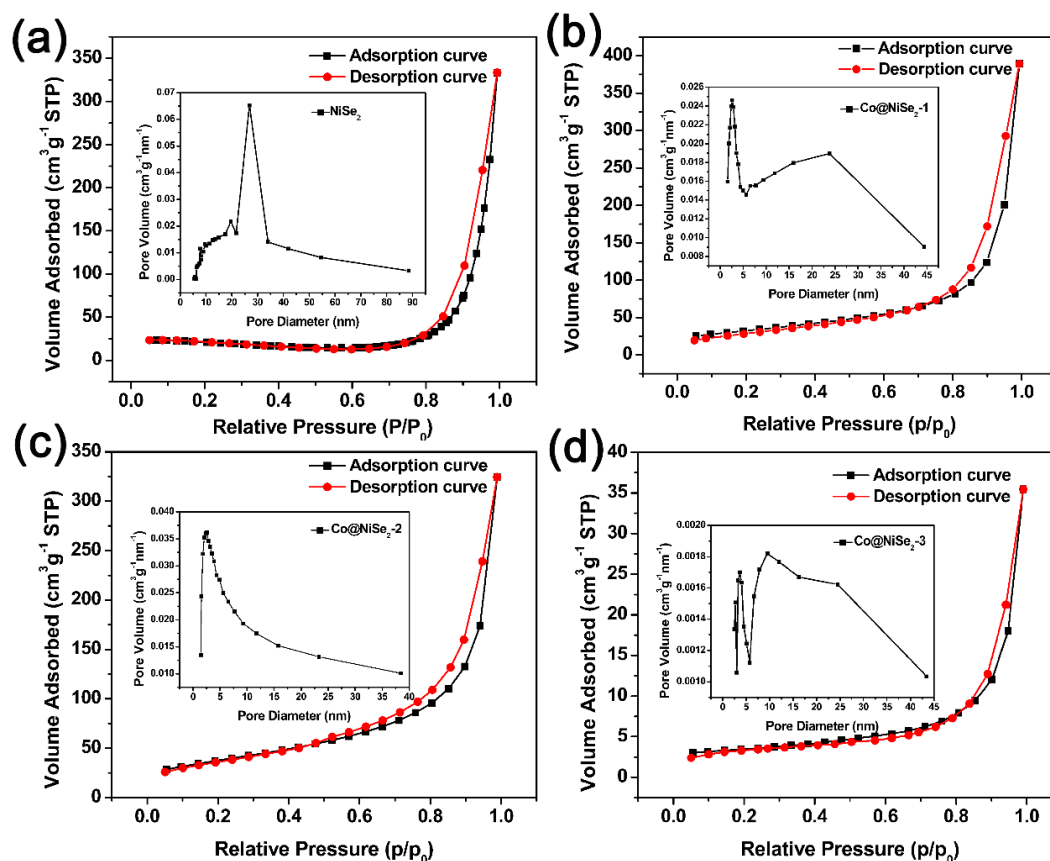


Figure 3. N_2 absorption–desorption curves and pore size distributions of (a) $NiSe_2$; (b) $Co@NiSe_2-1$; (c) $Co@NiSe_2-2$; and (d) $Co@NiSe_2-3$ electrode materials.

Table 1. Comparisons of surface area analysis of different electrode materials.

Sample	BET ($m^2 \cdot g^{-1}$)	Pore Volume ($cm^3 \cdot g^{-1}$)	Pore Size (nm)
$NiSe_2$	54.6	0.5	>30
$Co@NiSe_2-1$	115.7	0.6	>25
$Co@NiSe_2-2$	135.2	0.5	>5
$Co@NiSe_2-3$	11.5	0.05	>25

3.2. Electrochemical Properties of Electrode Materials

Electrochemical Tests of Electrode Materials in a Three-Electrode System

Figure 4 shows the electrochemical performance of a three-electrode system for $NiSe_2$ and Co-doped $NiSe_2$ electrode materials in 3 M KOH electrolyte. Figure 4a illustrates their CV curves at a scan rate of $5 \text{ mV} \cdot \text{s}^{-1}$ and a potential of 0–0.6 V (vs. Hg/HgO). A reversible redox peak is observed in the curves during charge and discharge. This phenomenon illustrates that the $NiSe_2$ and Co-doped $NiSe_2$ electrode materials show typical pseudocapacitance characteristics, and the CV curve of $Co@NiSe_2-2$ surrounds the largest area, indicating that this electrode material can produce the biggest specific capacitance. Figure 4b shows GCD curves of $NiSe_2$ and Co-doped $NiSe_2$ electrode materials at a current density of $1 \text{ A} \cdot \text{g}^{-1}$. According to these GCD curves, their specific capacitances are calculated. For $NiSe_2$, $Co@NiSe_2-1$, $Co@NiSe_2-2$, and $Co@NiSe_2-3$ electrode materials, the specific capacitances are 1091.3, 1249.6, 3167.6, and 580.4 $\text{F} \cdot \text{g}^{-1}$, respectively. The enhancement of the specific capacitance after doping with Co^{2+} is possibly due to the increase in the specific surface area of the electrode material and the synergistic effects of Co^{2+} and Ni^{2+} . This super high capacitance of the

Co@NiSe₂-2 electrode material is higher than those of the previously reported metal selenide electrodes and some other typical electrode materials, as shown in Table 2.

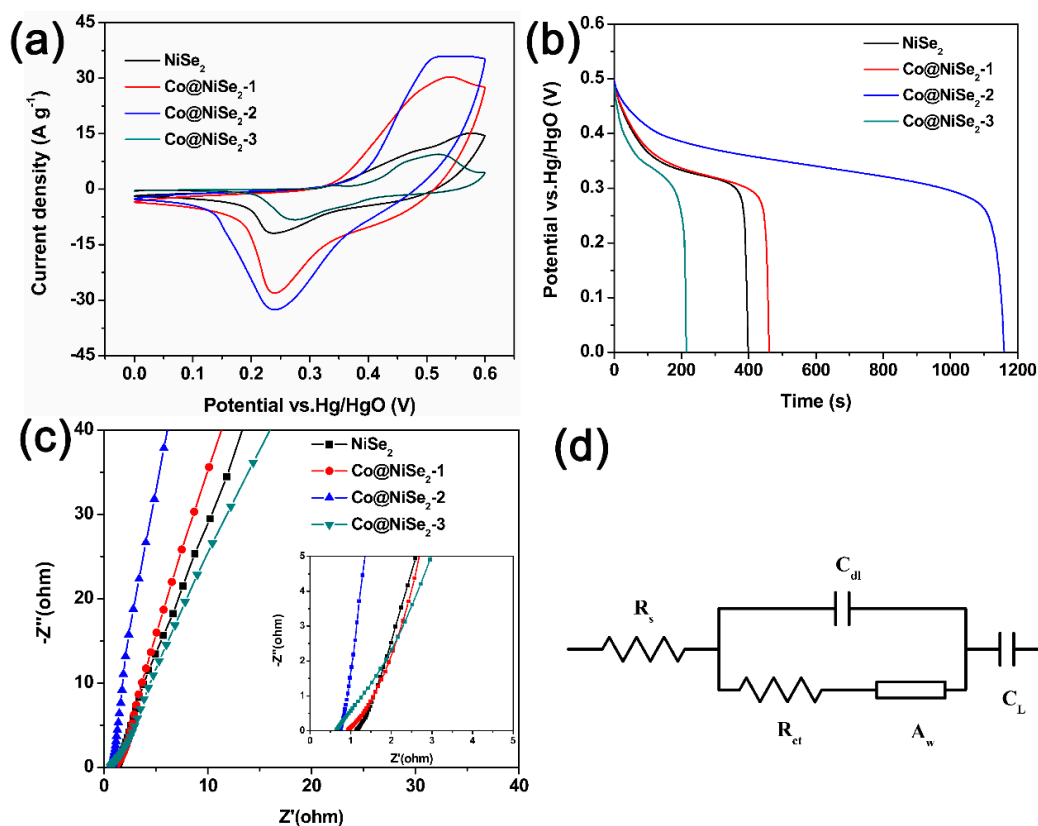


Figure 4. (a) Cyclic voltammetry (CV) curves of electrode materials at a scan rate of $5 \text{ mV}\cdot\text{s}^{-1}$; (b) galvanostatic charge-discharge (GCD) curves of electrode materials at a current density of $1 \text{ A}\cdot\text{g}^{-1}$; (c) Nyquist plots of electrode materials (the inset is the enlarged curves at a high-frequency curve range); (d) equivalent circuit used to fit the Nyquist spectra.

Table 2. Comparisons of supercapacitor performances with past typical materials.

Electrode Material	Electrolyte	Morphology Structure	Specific Capacitance ($\text{F}\cdot\text{g}^{-1}$)	Ref.
Co ₃ O ₄ /rGO	2 M KOH	Cubic morphology	487 $\text{F}\cdot\text{g}^{-1}$ at $5 \text{ mV}\cdot\text{s}^{-1}$	[33]
NiO	2 M KOH	Nanosheet hollow spheres	600 $\text{F}\cdot\text{g}^{-1}$ at $10 \text{ A}\cdot\text{g}^{-1}$	[34]
PANI/MoS _X	1 M H ₂ SO ₄	Nanoparticle	48.64 $\text{mF}\cdot\text{cm}^{-2}$ at $56.62 \mu\text{A}\cdot\text{cm}^{-2}$	[35]
GO/PPy	1 M Na ₂ SO ₄	Nanoparticle	332.6 $\text{F}\cdot\text{g}^{-1}$ at $0.25 \text{ A}\cdot\text{g}^{-1}$	[36]
NiS	3 M KOH	Microflower	1122.7 $\text{F}\cdot\text{g}^{-1}$ at $1 \text{ A}\cdot\text{g}^{-1}$	[37]
CoS	6 M KOH	Nanotubes	285 $\text{F}\cdot\text{g}^{-1}$ at $0.5 \text{ A}\cdot\text{g}^{-1}$	[38]
NiTe	3 M KOH	Nanorods	804 $\text{F}\cdot\text{g}^{-1}$ at $1 \text{ A}\cdot\text{g}^{-1}$	[39]
CoSe/C	2 M KOH	Nanoparticles	726 $\text{F}\cdot\text{g}^{-1}$ at $1 \text{ A}\cdot\text{g}^{-1}$	[20]
NiSe ₂	4 M KOH	Nano cube	1044 $\text{F}\cdot\text{g}^{-1}$ at $3 \text{ A}\cdot\text{g}^{-1}$	[18]
MoSe ₂	6 M KOH	Nanosheets	1114.3 $\text{F}\cdot\text{g}^{-1}$ at $1 \text{ A}\cdot\text{g}^{-1}$	[19]
Co-doped NiSe ₂	3 M KOH	Nanowire	3167.6 $\text{F}\cdot\text{g}^{-1}$ at $1 \text{ A}\cdot\text{g}^{-1}$	This work

Figure 4c displays the Nyquist plots of NiSe₂ and Co-doped NiSe₂ electrode materials. Impedance testing is a characterization of the dynamic characteristics between the electrode material and the electrolyte [40]. Table 3 shows comparisons of the impedance data of different electrode materials. R_s is related to the resistances of the current collector, the electrode material, and the electrolyte. R_{ct} represents the charge transfer resistance. Z_w refers to the ion diffusion resistance in the electrolyte. As can be seen from Table 3, Co@NiSe₂-2 has the smallest R_s ($0.72 \Omega\cdot\text{cm}^2$), R_{ct}

($0.82 \Omega \cdot \text{cm}^2$), and Z_w ($0.0012 \Omega \cdot \text{s}^{-1/2} \cdot \text{cm}^2$), which are beneficial; therefore, Co@NiSe₂-2 exhibits superior electrochemical performances. This indicates that the Co@NiSe₂-2 electrode has the best electronic conductivity and the fastest charge transfer rate. Therefore, we chose a Co@NiSe₂-2 electrode material for the following in-depth study.

Table 3. Comparisons of impedance data of different electrode materials.

Sample	R_s ($\Omega \cdot \text{cm}^2$)	R_{ct} ($\Omega \cdot \text{cm}^2$)	Z_w ($\Omega \cdot \text{s}^{-1/2} \cdot \text{cm}^2$)
NiSe ₂	1.14	1.45	0.0013
Co@NiSe ₂ -1	0.93	1.48	0.0026
Co@NiSe ₂ -2	0.72	0.82	0.0012
Co@NiSe ₂ -3	0.86	1.11	0.0015

Figure 5 describes the electrochemical tests of a Co@NiSe₂-2 electrode material in a 3 M KOH electrolyte using a three-electrode system. Figure 5a shows the CV curves at different scan rates (5–50 $\text{mV} \cdot \text{s}^{-1}$) for a Co@NiSe₂-2 electrode at a potential of 0–0.6 V vs Hg/HgO. The charge and discharge curves show a pair of reversible redox peaks, indicating that the Co@NiSe₂-2 electrode exhibits typical pseudocapacitance properties. With the increase of the scanning rate, the redox peak reveals a potential shift, but the shape of the curve does not change significantly. The change signifies that the electrode material not only had good reversibility but can also work stably at a potential window of 0–0.6 V vs Hg/HgO [41]. Figure 5b shows the plot of the square root of the scan rate and the peak current. This figure illustrates that both the oxidation peak and the reduction peak have an approximately linear relationship with the square root of the scan rate. This condition demonstrates the redox reaction at the electrolyte/electrode interface, corresponding to quasi reversible and diffusion control processes [42]. Figure 5c shows the GCD curves of the Co@NiSe₂-2 electrode in a potential window of 0–0.5 V vs Hg/HgO at different current densities. The GCD curves show that each line does not change linearly. Distinct charging and discharging platforms are observed due to reversible oxidation and reduction. Using the integral calculation Formula (3) to calculate the specific capacitances of the Co@NiSe₂-2 electrodes, the results are 3167.6, 2697.6, 2079.4, 1572.9, 1202.4, and 885.6 $\text{F} \cdot \text{g}^{-1}$ at current densities of 1, 2, 4, 6, 10, and 15 $\text{A} \cdot \text{g}^{-1}$, respectively, as shown in Figure 5d. As the current density increases, the capacitance declines, signifying that the kinetics of the redox reaction depend primarily on the diffusion and migration of ions in the electrolyte [43]. The migration and diffusion rates of electrolyte ions were suppressed at high current densities.

After the three-electrode test on the Co@NiSe₂-2 electrode material, we will use the AC electrode as the negative electrode and the Co@NiSe₂-2 electrode as the positive electrode to fabricate an asymmetric supercapacitor. The electrochemical performance of the capacitor will be further explored and analyzed.

Figure 6 is a comparison of the CV curves of an AC electrode and a Co@NiSe₂-2 electrode at a scan rate of 5 $\text{mV} \cdot \text{s}^{-1}$ in a three-electrode system. As can be seen from the figure, the potential window of the AC electrode is -1 – 0 V, and the AC electrode exhibits typical double-layer capacitance characteristics, whereas the potential window of the Co@NiSe₂-2 electrode was 0–0.6 V, showing a satisfying pseudocapacitance performance.

The asymmetric supercapacitor was composed of an AC electrode as the negative electrode and a Co@NiSe₂-2 electrode as the positive electrode. These two electrodes have a different energy storage mechanism, potential window, and specific capacitance; thus, they must be in accordance with the principle of charge storage [44]. At a current density of 1 $\text{A} \cdot \text{g}^{-1}$, the specific capacitances of the Co@NiSe₂-2 electrode and the AC electrode are 3167.6 and 253.6 $\text{F} \cdot \text{g}^{-1}$, respectively. Therefore, according to Formula (2) for the calculation of the quality of the AC electrode, we determined the best quality ratio of positive and negative materials as approximately $m(\text{Co@NiSe}_2\text{-2})/m(\text{AC}) = 0.16$ and assembled them into an asymmetric supercapacitor for testing.

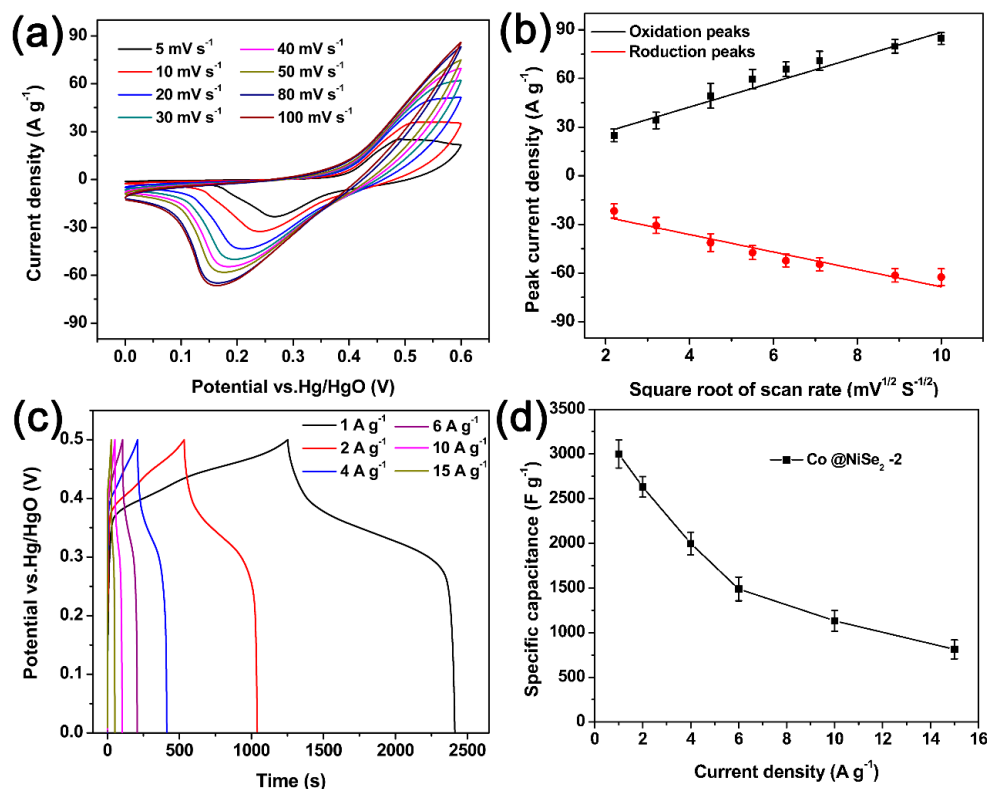


Figure 5. (a) CV curves of Co@NiSe₂-2 electrode at different scan rates; (b) relationship of the square root of the scan rate and the peak current; (c) GCD curves of Co@NiSe₂-2 electrode at different current densities; (d) specific capacitance of Co@NiSe₂-2 electrode at different current densities.

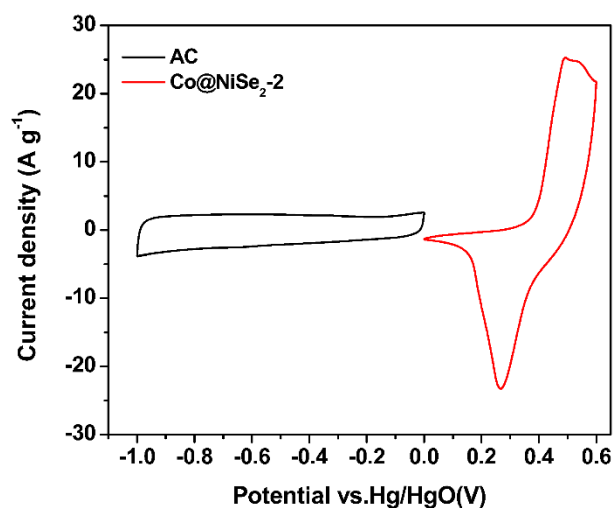


Figure 6. CV curves of the activated carbon (AC) electrode and the Co@NiSe₂-2 electrode in a three-electrode system.

Figure 7a shows the CV curves for the Co@NiSe₂-2//AC asymmetric supercapacitor at different potential windows and a scan rate of 50 mV·s⁻¹. Notably, the CV curve maintains a similar shape in the potential window of 1 to 1.6 V. When the potential window extends to 1.8 V, a polarized phenomenon appears. Thus, we can confirm that the asymmetric supercapacitor can be stabilized in the potential window of 0 to 1.6 V. From the analysis results of the CV curves, we specify the subsequent test potential window from 0 to 1.6 V. Figure 7b shows the GCD curves of the Co@NiSe₂-2//AC asymmetric

supercapacitor at a current density of $1 \text{ A}\cdot\text{g}^{-1}$ under different potential windows. As can be seen from the figure, all curves show exceptional consistency once again. The results show that the $\text{Co@NiSe}_2\text{-2}$ electrode has excellent electrochemical performance and stability. Figure 7c reveals the plots of specific capacitances for $\text{NiSe}_2//\text{AC}$ and $\text{Co@NiSe}_2\text{-2}//\text{AC}$ asymmetric supercapacitors at different potential windows. For both asymmetric supercapacitors, the specific capacitances increase with the increment of potential window. For the $\text{Co@NiSe}_2\text{-2}//\text{AC}$ asymmetric supercapacitor, when the potential window is from 1 to 1.6 V, the specific capacitance is enhanced from 70.64 to $136.06 \text{ F}\cdot\text{g}^{-1}$. Both the original and enhanced specific capacitances of the $\text{Co@NiSe}_2\text{-2}//\text{AC}$ asymmetric supercapacitor are much higher than those of $\text{NiSe}_2//\text{AC}$ (from 18.16 to $71.31 \text{ F}\cdot\text{g}^{-1}$). Figure 7d shows CV curves of $\text{Co@NiSe}_2\text{-2}//\text{AC}$ at different scanning rates of $10\text{--}100 \text{ mV}\cdot\text{s}^{-1}$ and with the same potential window of $0\text{--}1.6 \text{ V}$. No significant deformation of the CV curve is observed as the scan rate increases. In addition, each curve presents a similar quasi-rectangular shape, indicating the cooperative behavior of pseudocapacitive $\text{Co@NiSe}_2\text{-2}$ electrode and the electric double-layer capacitive AC electrode. In addition, this phenomenon indicates that this asymmetric supercapacitor has rapid charge–discharge reversibility. Figure 7e shows GCD curves of the $\text{Co@NiSe}_2\text{-2}//\text{AC}$ asymmetric supercapacitor at different current densities. The specific capacitances at current densities of 1, 2, 4, 5, and $6 \text{ A}\cdot\text{g}^{-1}$ are 140.6, 121.2, 98, 88.7, and $80.6 \text{ F}\cdot\text{g}^{-1}$, respectively. The specific capacitance for the $\text{Co@NiSe}_2\text{-2}//\text{AC}$ asymmetric supercapacitor at $6 \text{ A}\cdot\text{g}^{-1}$ is 57.3% of that at $1 \text{ A}\cdot\text{g}^{-1}$ in the case of a sixfold increase in the current density, which is higher than that for the $\text{NiSe}_2//\text{AC}$ asymmetric supercapacitor (38.9%), demonstrating that the assembled $\text{Co@NiSe}_2\text{-2}//\text{AC}$ asymmetric supercapacitor presents a good rate performance, as shown in Figure 7f.

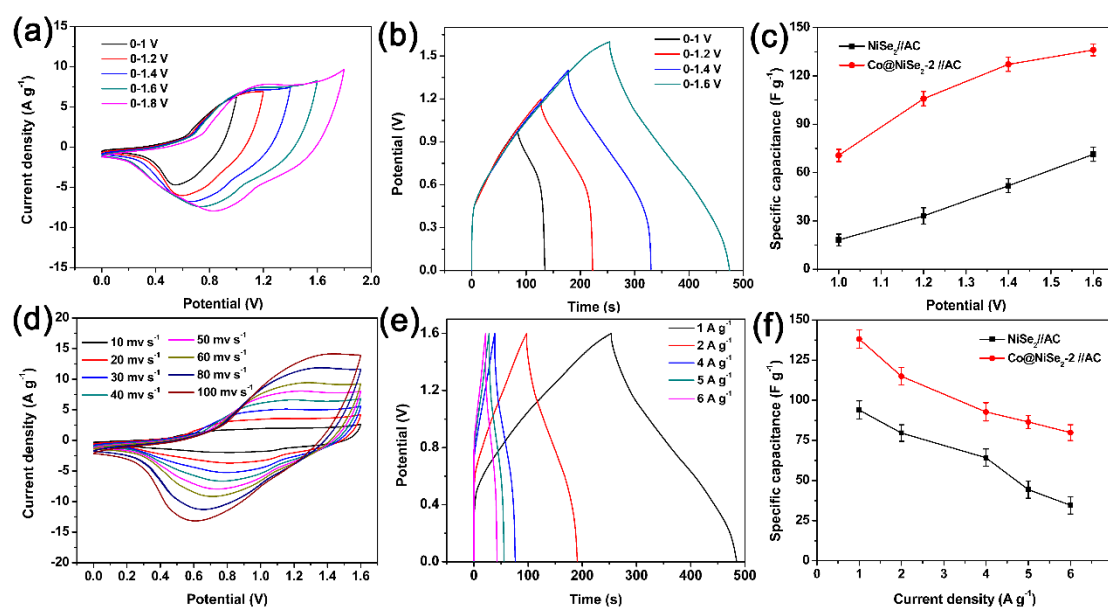


Figure 7. (a) CV curves of $\text{Co@NiSe}_2\text{-2}//\text{AC}$ asymmetric supercapacitor at a scan rate of $50 \text{ mV}\cdot\text{s}^{-1}$ at different potential windows; (b) GCD curves of $\text{Co@NiSe}_2\text{-2}//\text{AC}$ asymmetric supercapacitor at different potential windows at a current density of $1 \text{ A}\cdot\text{g}^{-1}$; (c) plots of specific capacitances for $\text{NiSe}_2//\text{AC}$ and $\text{Co@NiSe}_2\text{-2}//\text{AC}$ asymmetric supercapacitors at different potential windows; (d) CV curves of $\text{Co@NiSe}_2\text{-2}//\text{AC}$ at different scanning rates; (e) GCD curves of $\text{Co@NiSe}_2\text{-2}//\text{AC}$ asymmetric supercapacitor at different current densities; (f) plots of specific capacitances for $\text{NiSe}_2//\text{AC}$, $\text{Co@NiSe}_2\text{-2}//\text{AC}$ asymmetric supercapacitors at different current densities.

Figure 8a shows the Ragone plots of $\text{NiSe}_2//\text{AC}$ and $\text{Co@NiSe}_2\text{-2}//\text{AC}$ asymmetric supercapacitors, which refer to the relationship of energy density and power density derived from GCD curves at different current densities. The $\text{Co@NiSe}_2\text{-2}//\text{AC}$ asymmetric supercapacitor can

reach the maximum energy density of $50 \text{ Wh}\cdot\text{kg}^{-1}$ at a power density of $779 \text{ W}\cdot\text{kg}^{-1}$, which exceeds that of the $\text{NiSe}_2//\text{AC}$ asymmetric supercapacitor ($34.8 \text{ Wh}\cdot\text{kg}^{-1}$ at $998 \text{ W}\cdot\text{kg}^{-1}$), and those of most previously reported NiSe_2 -based supercapacitors [18–20]. Figure 8b shows the cycle life for $\text{NiSe}_2//\text{AC}$ and $\text{Co@NiSe}_2\text{-2//AC}$ asymmetric supercapacitors over 4000 charge-discharge cycles at a constant current density of $1 \text{ A}\cdot\text{g}^{-1}$. Both capacitors exhibit an increase in capacitance in the first 200 cycles, which is assigned to the activation process [45], and then present a decrease in capacitance. After 4000 cycles, the capacitance retention rate for the $\text{Co@NiSe}_2\text{-2//AC}$ asymmetric supercapacitor is 79.4%, which is higher than that of the $\text{NiSe}_2//\text{AC}$ asymmetric supercapacitor (57.9%), indicating good cycling stability.

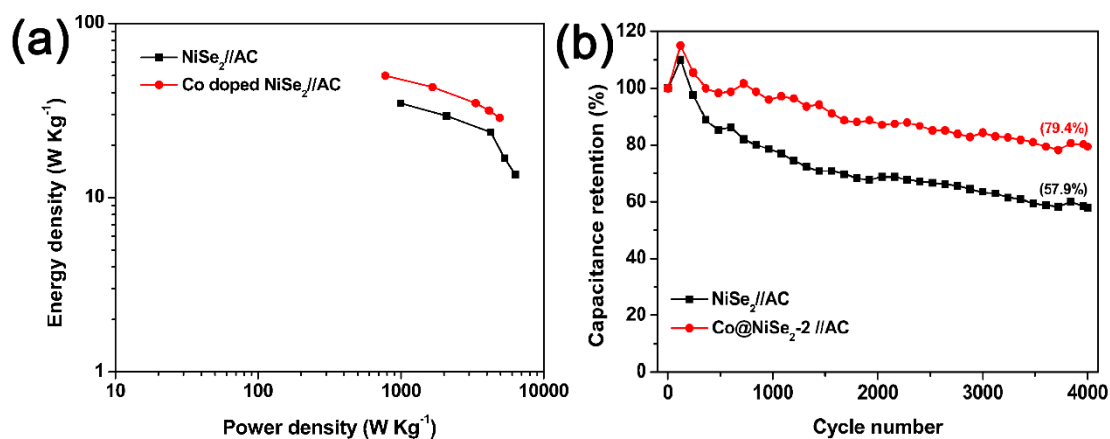


Figure 8. (a) Ragone plots; (b) cyclic performances tested at a current density of $1 \text{ A}\cdot\text{g}^{-1}$ of $\text{NiSe}_2//\text{AC}$ and $\text{Co@NiSe}_2\text{-2//AC}$ asymmetric supercapacitors.

The possible reasons for the superior electrochemical performances of $\text{Co@NiSe}_2\text{-2//AC}$ asymmetric supercapacitor are shown as follows: 1) This unique nanowire structure is beneficial to the transfer of electrons; 2) the doping of Co^{2+} into NiSe_2 can increase the specific surface area, leading to an increase in the use of active material; 3) the direct growth of the electrode material onto the current collector (Ni foam) does not require extra binder and conductive additive, avoiding a decline in the electrochemical performance caused by obstruction of the hole in the electrode material.

4. Conclusions

The Co@NiSe_2 electrode material with a nanowire structure was synthesized by a simple one-step hydrothermal method with nickel foam as the supporter. Proper doping of Co^{2+} into NiSe_2 can greatly improve the electrochemical performances of electrode material. The specific capacitance of the $\text{Co@NiSe}_2\text{-2}$ electrode can reach up to $3167.6 \text{ F}\cdot\text{g}^{-1}$ at the current density of $1 \text{ A}\cdot\text{g}^{-1}$. This $\text{Co@NiSe}_2\text{-2}$ electrode as the positive electrode assembled with AC as the negative electrode lead to a $\text{Co@NiSe}_2\text{-2//AC}$ asymmetric supercapacitor. The asymmetric supercapacitor can reversibly work in the potential window of 0–1.6 V, shows a high energy density of $50 \text{ Wh}\cdot\text{kg}^{-1}$ at a power density of $779 \text{ W}\cdot\text{kg}^{-1}$. In addition, after 4000 charge-discharge cycles, a retention rate of 79.4% can be achieved. The results show that the obtained $\text{Co@NiSe}_2\text{-2}$ electrode material has potential as a supercapacitor electrode material.

Author Contributions: Design and Preparation, Y.G. and L.-Q.F.; Conceptualization, G.-L.G.; Methodology, J.-L.H.; Investigation, M.-L.H.; Formal Analysis, Y.-F.H. and J.-M.L.; Writing-Original Draft Preparation, Y.G.; Writing-Review & Editing, L.-Q.F.; Funding Acquisition, J.-H.W. and L.-Q.F.

Funding: This research was funded by the National Natural Science Foundation of China (No. 21301060), the Natural Science Foundation of Fujian Province (No. 2017J01084), the Graphene Powder & Composite Research Center of Fujian Province (No. 2017H21010008), the Program for New Century Excellent Talents in Fujian Province University (No. 2014FJ-NCET-ZR02), the Scientific Research Foundation for the Returned Overseas Chinese

Scholars, State Education Ministry, and the Cultivation Program for Postgraduate in scientific Research Innovation Ability of Huaqiao University (No. 1611302006).

Conflicts of Interest: The authors declare no conflict of interest.

References

1. Bruce, P.G.; Freunberger, S.A.; Hardwick, L.J.; Tarascon, J.M. Li-O₂ and Li-S batteries with high energy storage. *Nat. Mater.* **2011**, *11*, 19–29. [[CrossRef](#)] [[PubMed](#)]
2. Li, Q.; Zheng, S.; Xu, Y.; Xue, H.; Pang, H. Ruthenium based materials as electrode materials for supercapacitors. *Chem. Eng. J.* **2017**, *333*, 505–518. [[CrossRef](#)]
3. Salanne, M.; Rotenberg, B.; Naoi, K.; Kaneko, K.; Taberna, P.L.; Grey, C.P.; Dunn, B.; Simon, P. Efficient storage mechanisms for building better supercapacitors. *Nat. Energy* **2016**, *1*, 16070. [[CrossRef](#)]
4. Daraghme, A.; Hussain, S.; Servera, L.; Xuriguera, E.; Cornet, A.; Cirera, A. Impact of binder concentration and pressure on performance of symmetric CNFs based supercapacitors. *Electrochim. Acta* **2017**, *245*, 531–538. [[CrossRef](#)]
5. Zhang, L.; Hu, X.; Wang, Z.; Sun, F.; Dorrell, D.G. A review of supercapacitor modeling, estimation, and applications: A control/management perspective. *Renew. Sustain. Energy Rev.* **2017**, *81*, 1868–1878. [[CrossRef](#)]
6. Wang, W.; Liu, W.Y.; Zeng, Y.X.; Han, Y.; Yu, M.H.; Lu, X.H.; Tong, Y.X. A novel exfoliation strategy to significantly boost the energy storage capability of commercial carbon cloth. *Adv. Mater.* **2015**, *27*, 3572–3578. [[CrossRef](#)] [[PubMed](#)]
7. Cakici, M.; Reddy, K.R.; Alonso, M.F. Advanced electrochemical energy storage supercapacitors based on the flexible carbon fiber fabric-coated with uniform coral-like MnO₂ structured electrodes. *Chem. Eng. J.* **2017**, *309*, 151–158. [[CrossRef](#)]
8. Hulicova, J.D.; Puziy, A.M.; Poddubnaya, O.I.; Suarez, G.F.; Juan, M.D.; Lu, G.Q. Highly Stable Performance of Supercapacitors from Phosphorus-Enriched Carbons. *J. Am. Chem. Soc.* **2009**, *131*, 5026–5027. [[CrossRef](#)] [[PubMed](#)]
9. Futaba, D.N.; Hata, K.; Yamada, T.; Hiraoka, T.; Hayamizu, Y.; Kakudate, Y.; Tanaike, O.; Hatori, H.; Yumura, M.; Iijima, S. Shape-engineerable and highly densely packed single-walled carbon nanotubes and their application as super-capacitor electrodes. *Nat. Mater.* **2006**, *12*, 987–994. [[CrossRef](#)] [[PubMed](#)]
10. Choi, B.G.; Yang, M.; Hong, W.H.; Choi, J.W.; Huh, Y.S. 3D Macroporous Graphene Frameworks for Supercapacitors with High Energy and Power Densities. *ACS Nano* **2012**, *6*, 4020–4028. [[CrossRef](#)] [[PubMed](#)]
11. Naderi, H.R.; Nasab, A.S.; Nasrabi, M.R.; Ganjali, M.R. Decoration of nitrogen-doped reduced graphene oxide with cobalt tungstate nanoparticles for use in high-performance supercapacitors. *Appl. Surf. Sci.* **2017**, *423*, 1025–1034. [[CrossRef](#)]
12. Miao, L.; Zhu, D.Z.; Zhao, Y.H.; Liu, M.X.; Duan, H.; Xiong, W.; Zhu, Q.J.; Li, L.C.; Gan, L.H. Design of carbon materials with ultramicro-, supermicro- and mesopores using solvent- and self-template strategy for supercapacitors. *Microporous Mesoporous Mater.* **2017**, *253*, 1–9. [[CrossRef](#)]
13. Yan, J.; Ren, C.E.; Maleski, K.; Hatter, C.B.; Anasori, B.; Urbankowski, P.; Sarycheva, A.; Gogotsi, Y. Flexible MXene/Graphene Films for Ultrafast Supercapacitors with Outstanding Volumetric Capacitance. *Adv. Funct. Mater.* **2017**, *27*, 1701264. [[CrossRef](#)]
14. Simon, P.; Gogotsi, Y. Materials for electrochemical capacitors. *Nat. Mater.* **2008**, *7*, 845–854. [[CrossRef](#)] [[PubMed](#)]
15. Fan, L.Q.; Liu, G.J.; Wu, J.H.; Liu, L.; Lin, J.M.; Wei, Y.L. Asymmetric supercapacitor based on graphene oxide/polypyrrole composite and activated carbon electrodes. *Electrochim. Acta* **2014**, *137*, 26–33. [[CrossRef](#)]
16. Fan, L.Q.; Liu, G.J.; Zhang, C.Y.; Wu, J.H.; Wei, Y.L. Facile one-step hydrothermal preparation of molybdenum disulfide/carbon composite for use in supercapacitor. *Int. J. Hydrogen Energy* **2015**, *40*, 10150–10157. [[CrossRef](#)]
17. You, B.; Sun, Y.J. Hierarchically porous nickel sulfide multifunctional superstructures. *Adv. Energy Mater.* **2016**, *6*, 1502333–1502341. [[CrossRef](#)]
18. Dong, X.; Wang, K.; Zhao, C.; Qian, X.; Chen, S.; Li, Z.; Liu, H.; Dou, S. Direct synthesis of RGO/Cu₂O composite films on Cu foil for supercapacitors. *J. Alloys Compd.* **2014**, *586*, 745–753. [[CrossRef](#)]

19. Wang, S.L.; Li, W.; Xin, L.P.; Wu, M.; Long, Y.; Huang, H.; Lou, X. Facile synthesis of truncated cube-like NiSe₂ single crystals for high-performance asymmetric supercapacitors. *Chem. Eng. J.* **2017**, *330*, 1334–1341. [[CrossRef](#)]
20. Huang, K.J.; Zhang, J.Z.; Fan, Y. Preparation of layered MoSe₂ nanosheets on Ni-foam substrate with enhanced supercapacitor performance. *Mater. Lett.* **2015**, *152*, 244–247. [[CrossRef](#)]
21. Zhang, Y.F.; Pan, A.Q.; Wang, Y.P.; Cao, X.X.; Zhou, Z.; Zhu, T.; Liang, S.; Cao, G. Self-templated synthesis of N-doped CoSe₂/C double-shelled dodecahedra for high-performance supercapacitors. *Energy Storage Mater.* **2017**, *8*, 28–34. [[CrossRef](#)]
22. Wang, Y.G.; Song, Y.F.; Xia, Y.Y. Electrochemical capacitors: Mechanism, materials systems, characterization and applications. *Chem. Soc. Rev.* **2016**, *45*, 5925–5950. [[CrossRef](#)] [[PubMed](#)]
23. Guo, K.L.; Cui, S.Z.; Hou, H.W.; Chen, W.H.; Mi, L. Hierarchical ternary Ni-Co-Se nanowires for high-performance supercapacitor device design. *Dalton Trans.* **2016**, *45*, 19458–19465. [[CrossRef](#)] [[PubMed](#)]
24. Yu, H.Y.; Wu, J.H.; Fan, L.Q.; Xu, K.Q.; Zhong, X.; Lin, Y.Z.; Lin, J.M. Improvement of the performance for quasi-solid-state supercapacitor by using PVA-KOH-KI polymer gel electrolyte. *Electrochim. Acta* **2011**, *56*, 6881–6886. [[CrossRef](#)]
25. Yang, H.Z. Estimation of Supercapacitor Charge Capacity Bounds Considering Charge Redistribution. *Chem. Eng. J.* **2018**, *345*, 186–195. [[CrossRef](#)]
26. Yan, J.; Fan, Z.; Wei, S.; Ning, G.Q.; Wei, T.; Zhang, Q.; Zhang, R.; Zhi, L.; Wei, F. Advanced Asymmetric Supercapacitors Based on Ni(OH)₂ /Graphene and Porous Graphene Electrodes with High Energy Density. *Adv. Funct. Mater.* **2012**, *22*, 2632–2641. [[CrossRef](#)]
27. Yan, J.; Wang, Q.; Wei, T.; Fan, Z. Recent Advances in Design and Fabrication of Electrochemical Supercapacitors with High Energy Densities. *Adv. Energy Mater.* **2014**, *4*, 1300816. [[CrossRef](#)]
28. Mai, L.Q.; Minhas-Khan, A.; Tian, X.; Hercule, K.M.; Zhao, Y.-L.; Lin, X.; Xu, X. Synergistic interaction between redox-active electrolyte and binder-free functionalized carbon for ultrahigh supercapacitor performance. *Nat. Commun.* **2013**, *4*, 2923–2925. [[CrossRef](#)] [[PubMed](#)]
29. Zhang, J.; Jiang, J.; Li, H.; Zhao, X.S. A high-performance asymmetric supercapacitor fabricated with graphene-based electrodes. *Energy Environ. Sci.* **2011**, *4*, 4009–4015. [[CrossRef](#)]
30. Tu, Q.M.; Fan, L.Q.; Pan, F.; Huang, J.L.; Gu, Y.; Lin, J.-M.; Huang, M.-L.; Huang, Y.-F.; Wu, J.-H. Design of a novel redox-active gel polymer electrolyte with a dual-role ionic liquid for flexible supercapacitors. *Electrochim. Acta* **2018**, *268*, 562–568. [[CrossRef](#)]
31. Saha, D.; Li, Y.C.; Bi, Z.H.; Chen, J.H.; Keum, J.K.; Hensley, D.K.; Grappe, H.A.; Meyer, H.M.; Dai, S.; Paranthaman, M.P.; et al. Studies on Supercapacitor Electrode Material from Activated Lignin-Derived Mesoporous Carbon. *Am. Chem. Soc.* **2014**, *30*, 900–910. [[CrossRef](#)] [[PubMed](#)]
32. Khan, A.H.; Ghosh, S.; Pradhan, B.; Dalui, A.; Shrestha, L.K.; Acharya, S.; Ariga, K. Two-Dimensional (2D) Nanomaterials towards Electrochemical Nanoarchitectonics in Energy-Related Applications. *Bull. Chem. Soc. Jpn.* **2017**, *90*, 627–648. [[CrossRef](#)]
33. Lee, J.S.; Kim, S.I.; Yoon, J.C.; Jang, J.H. Chemical Vapor Deposition of Mesoporous Graphene Nanoballs for Supercapacitor. *ACS Nano* **2013**, *7*, 6047–6055. [[CrossRef](#)] [[PubMed](#)]
34. Sengottaiyan, C.; Jayavel, R.; Bairi, P.; Shrestha, R.G.; Ariga, K.; Shrestha, L.K. Cobalt Oxide/Reduced Graphene Oxide Composite with Enhanced Electrochemical Supercapacitance Performance. *Bull. Chem. Soc. Jpn.* **2017**, *90*, 955–962. [[CrossRef](#)]
35. Yu, W.; Jiang, X.; Ding, S.; Li, B.Q. Preparation and electrochemical characteristics of porous hollow spheres of NiO nanosheets as electrodes of supercapacitors. *J. Power Sources* **2014**, *256*, 440–448. [[CrossRef](#)]
36. Wang, Y.; Mayorga-Martinez, C.C.; Pumera, M. Polyaniline/MoS_x Supercapacitor by Electrodeposition. *Bull. Chem. Soc. Jpn.* **2017**, *90*, 847–853. [[CrossRef](#)]
37. Guan, B.; Li, Y.; Yin, B.; Liu, K.; Wang, D.; Zhang, H.; Cheng, C. Synthesis of hierarchical NiS microflowers for high performance asymmetric supercapacitor. *Chem. Eng. J.* **2017**, *308*, 1165–1173. [[CrossRef](#)]
38. Pang, H.; Wei, C.; Li, X.; Li, G.; Ma, Y.; Li, S.; Chen, J.; Zhang, J. Microwave-assisted synthesis of NiS₂ nanostructures for supercapacitors and cocatalytic enhancing photocatalytic H₂ production. *Sci. Rep.* **2014**, *4*, 3577. [[CrossRef](#)] [[PubMed](#)]
39. Wan, H.; Ji, X.; Jiang, J.; Yu, J.; Miao, L.; Bie, S.; Chen, H.; Ruan, Y. Hydrothermal synthesis of cobalt sulfide nanotubes: The size control and its application in supercapacitors. *J. Power Sources* **2013**, *243*, 396–402. [[CrossRef](#)]

40. Zhou, P.; Fan, L.; Wu, J.; Gong, C.; Zhang, J.; Tu, Y. Facile hydrothermal synthesis of NiTe and its application as positive electrode material for asymmetric supercapacitor. *J. Alloys Compd.* **2016**, *685*, 384–390. [[CrossRef](#)]
41. Dubal, D.P.; Lee, S.H.; Kim, J.G.; Kim, W.B.; Lokhande, C.D. Porous polypyrrole clusters prepared by electropolymerization for a high performance supercapacitor. *J. Mater. Chem.* **2012**, *22*, 3044–3052. [[CrossRef](#)]
42. Wang, H.; Casalongue, H.S.; Liang, Y.; Dai, H. Ni(OH)₂ nanoplates grown on graphene as advanced electrochemical pseudocapacitor materials. *J. Am. Chem. Soc.* **2010**, *132*, 7472–7477. [[CrossRef](#)] [[PubMed](#)]
43. Zhu, Y.; Ji, X.; Chen, H. The investigation of the electrochemically supercapacitive performances of mesoporous CuCo₂S₄. *RSC Adv.* **2016**, *6*, 84236–84241. [[CrossRef](#)]
44. Zhang, G.Q.; Lou, X.W. General Solution Growth of Mesoporous NiCo₂O₄ Nanosheets on Various Conductive Substrates as High-Performance Electrodes for Supercapacitors. *Adv. Mater.* **2013**, *25*, 976–979. [[CrossRef](#)] [[PubMed](#)]
45. Chen, F.S.; Wang, H.; Ji, S.; Linkov, V.; Wang, R. Core-shell structured Ni₃S₂@Co(OH)₂ nano-wires grown on Ni foam as binder-free electrode for asymmetric supercapacitors. *Chem. Eng. J.* **2018**, *345*, 48–57. [[CrossRef](#)]



© 2018 by the authors. Licensee MDPI, Basel, Switzerland. This article is an open access article distributed under the terms and conditions of the Creative Commons Attribution (CC BY) license (<http://creativecommons.org/licenses/by/4.0/>).